International Journal of Computer Science and Information Technology

ISSN: 3005-9682 (Print), ISSN: 3005-7140 (Online) | Volume 6, Number 2, Year 2025

DOI: https://doi.org/10.62051/ijcsit.v6n2.06

Journal homepage: https://wepub.org/index.php/IJCSIT/index

A Composite Sensor Calibration Algorithm Based on Deep Neural Network

Sibo Li, Fan Wei

Xi'an Shiyou University, Xi'an 710065, China

ABSTRACT

Accurate vacuum measurement is critical in numerous fields. Aiming at the issues of nonlinear errors, temperature drift, and gas composition interference in the overlapping region of Pirani and piezoresistive composite vacuum sensors, this paper proposes an adaptive calibration algorithm based on a hysteresis-type deep neural network (H-DNN). Through analyzing the structure and principle of the composite sensor, it is found that the quadratic nonlinear characteristics of the piezoresistive sensor in the overlapping region significantly differ from the logarithmic response of the Pirani sensor. Moreover, a temperature fluctuation of 10°C can cause the error of the former to change by ±0.8% and that of the latter by ±1.2%, while gas composition changes can make the Pirani error reach up to 15%. To address these challenges, a four-level algorithm framework is designed, and a hysteresis-type deep neural network architecture for the overlapping segment is constructed. By employing a bidirectional feedback mechanism and multi-physical-field coupling modeling, environmental interference suppression and dynamic weight allocation are achieved. Experimental results show that this algorithm reduces the long-term stability error in the overlapping region from ±5.0% to ±0.8%. Full-range verification indicates that after calibration, the error in the overlapping region is ≤±1%, and the errors of the Pirani and piezoresistive sensors in the non-overlapping regions are reduced to ±3% and ±4%, respectively. This significantly enhances the reliability of composite sensors under complex working conditions and provides an efficient solution for wide-range vacuum measurement in fields such as semiconductor manufacturing and aerospace exploration.

KEYWORDS

Composite vacuum sensor; Overlapping segment calibration; Dynamic compensation; Deep neural network

1. INTRODUCTION

In high-precision industrial and research fields such as semiconductor manufacturing, aerospace exploration, and vacuum coating, wide-range and highly reliable vacuum measurement is a core component for ensuring process stability and data accuracy [1]. Traditional single-type vacuum sensors struggle to cover the full range from high to low vacuum due to their limited measurement spans, while composite sensors—by integrating Pirani and piezoresistive sensors and utilizing the overlapping range of the two to achieve wide-range connection—have become a current research hotspot. However, such composite sensors face multiple technical challenges in the overlapping region: First, there are significant differences in nonlinear characteristics. The piezoresistive sensor exhibits quadratic nonlinear errors near 1000 mbar due to the elastic limit of the silicon diaphragm material based on the strain effect [2]. The Pirani sensor, relying on gas thermal conduction, shows logarithmic response characteristics in the medium-pressure range and has weak stability due to gas molecular thermal motion, leading to obvious data jumps in the overlapping region. Second, they are sensitive to environmental interference. Temperature fluctuations affect the two types of sensors differently. For every 10°C change in temperature, the Pirani sensor has an error variation of ±1.2% due to thermal conductivity coefficient drift [3], while the piezoresistive sensor has an error of ±0.8% due to changes in the Young's modulus of the silicon diaphragm. Existing calibration algorithms based on fixed mathematical models struggle to dynamically adapt to the above nonlinear characteristics and time-varying interference, resulting in long-term stability errors of up to ±5.0% in the overlapping region, which seriously restricts the application of composite sensors in complex working conditions [4]. To address this situation, this paper proposes an adaptive calibration algorithm based on a hysteresis-type deep neural network (H-DNN) with a lightweight network architecture: the hysteresis-type deep neural network for the overlapping segment is used to extract frequency-domain features through convolutional layers, fit nonlinear characteristics through fully connected layers, and ensure real-time performance on embedded edge devices (calibration delay <5 ms) using model compression techniques. Experimental results show that the algorithm reduces the error in the overlapping region from ±5.0% to ±0.8%, significantly improving the full-range measurement accuracy, providing an efficient solution for wide-range vacuum measurement, and being of great significance for promoting technological progress in fields such as semiconductor process optimization and spacecraft vacuum environment simulation.

2. SENSOR STRUCTURE AND PRINCIPLE

2.1. Principle and Structure of Pirani Sensor

The Pirani sensor is a typical device for thermal conductivity vacuum measurement, with its core principle based on the dynamic relationship between the thermal conductivity of gas molecules and pressure [1]. The sensor typically consists of a metal resistance wire (such as tungsten or platinum) or a thin-film structure, which inversely calculates the environmental pressure by monitoring the resistance change of the thermal-sensitive element through a Wheatstone bridge or constant-temperature circuit [6]. When the thermal-sensitive element is electrically heated to a constant temperature (150–300°C), the heat loss in its thermal equilibrium state is directly related to the collision frequency of surrounding gas molecules. In a low-vacuum environment (10^1–10^3 Pa), the gas molecular density is high, heat conduction is dominated by molecular collisions, and heat loss increases approximately linearly with rising pressure [7]. In the high-vacuum region ($<10^{-1}$ Pa), the molecular mean free path is much larger than the structural size, and heat loss shifts to radiation and thermal conduction through the support structure, resulting in significantly reduced sensitivity to pressure changes. Its pressure inversion model can be expressed as:

$$P = \mathrm{K}(t) * \left(\frac{V^2}{R} - Q_{rad}\right) \tag{1}$$

Where $\mathrm{K}(t)$is the temperature-dependent thermal conductivity coefficient, Q_{rad} is the radiative heat loss, V is the heating voltage, and$R$ is the resistance value of the thermal-sensitive element.

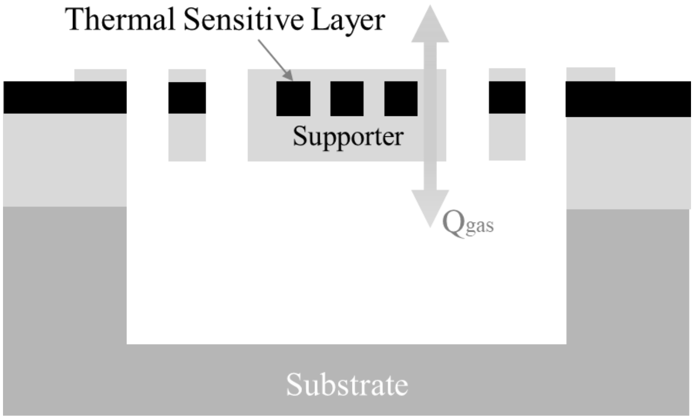

Figure 1. Schematic diagram of the Pirani sensor chip structure

2.2. Principle and Structure of Piezoresistive Sensor

The piezoresistive sensor relies on the piezoresistive effect of semiconductor materials to measure vacuum degree by detecting the characteristic that the resistance value of the pressure-sensitive element changes with pressure [8]. Its core structure is a pressure-sensitive element (such as a silicon diaphragm) made of semiconductor materials like monocrystalline silicon. Through MEMS (Micro-Electro-Mechanical Systems) processes, thin films or cantilever beam structures are fabricated on the silicon wafer, and piezoresistive films are formed via diffusion or ion implantation in specific regions, connected in the form of a Wheatstone bridge [9]. When external pressure acts on the silicon diaphragm, the diaphragm produces strain, causing changes in the lattice structure of the piezoresistive films, and the resistance values change accordingly [10]. According to Hooke's law and the piezoresistive properties of semiconductors, within a certain pressure range, the change in resistance is proportional to the pressure [11]. The relationship between the output voltage signal of the Wheatstone bridge and pressure is expressed as:

$$\Delta V = V_{ex} * \frac{\left(\frac{\Delta R_1}{R_1} - \frac{\Delta R_2}{R_2} + \frac{\Delta R_3}{R_3} - \frac{\Delta R_4}{R_4}\right)}{4} \tag{2}$$

Where V_{ex} is the excitation voltage, and ΔRi is the relative resistance change of each bridge arm.

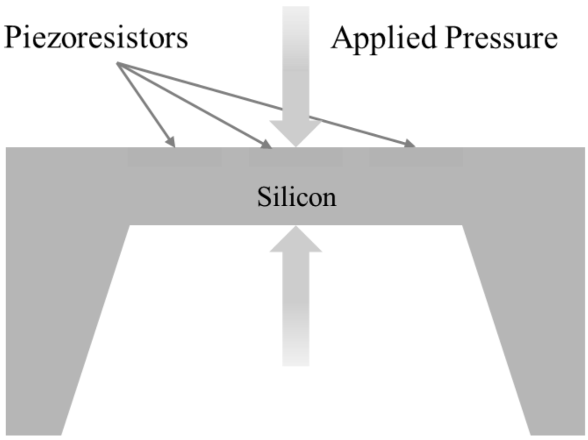

Figure 2. Schematic diagram of the piezoresistive sensor chip structure

2.3. Analysis of Overlapping Region Characteristics

The overlapping region of Pirani and piezoresistive sensors is 50–1000 mbar, serving as a critical area for range connection and directly influencing the full-range measurement accuracy and continuity of composite sensors. As shown in the data of Fig. 3, within this overlapping region, the piezoresistive sensor exhibits nonlinear voltage growth with increasing pressure due to the strain effect of the silicon diaphragm. The Pirani sensor, relying on gas thermal conduction, shows a rapid voltage rise after pressure reaches a certain threshold. In terms of characteristics, the piezoresistive sensor has relatively good linearity in the medium-low pressure segment (near 50 mbar), but as pressure approaches 1000 mbar, the deformation of the silicon diaphragm approaches its elastic limit, leading to increased nonlinear errors. The Pirani sensor is responsive in the medium-pressure segment but has slightly weaker data stability due to complex gas molecular thermal motion.

For quantitative analysis, multiple data sets within the 50–1000 mbar overlapping region were collected, and key indicators are summarized in Table 1:

Table 1. Key indicators of the composite sensor

Sensor Type	Output Voltage Range (V)	Fitting Model Characteristics	Typical Error Rate	Temperature Influence Trend
Pirani	0.5–4.5	Higher pressure leads to faster voltage rise	±3.8%	Increased temperature causes error due to thermal conductivity drift
Piezoresistive	1.2–4.2	Quadratic nonlinearity between pressure and voltage	±5.2%	Temperature alters piezoresistive coefficient, causing error fluctuations

Environmental factors significantly interfere with the overlapping region: a temperature fluctuation of 10°C increases the output error of the Pirani sensor by approximately ±1.2% due to changes in thermal conductivity coefficients [12, 13], while the piezoresistive sensor experiences ±0.8% error variation due to the Young's modulus of the silicon diaphragm. Additionally, changes in gas composition (e.g., hydrogen contamination) can cause abnormal thermal conductivity variations in the Pirani sensor (with a maximum deviation of 15%), whereas the piezoresistive sensor is unaffected by gas types [14].

Calibrating the overlapping region requires overcoming three major challenges: 1) establishing dynamic mapping between the logarithmic response of the Pirani sensor and the quadratic nonlinearity of the piezoresistive sensor to adapt to characteristic differences [15]; 2) real-time compensation for cross-interference from temperature and gas composition; and 3) dynamic allocation of fusion weights based on sensor confidence levels. The hysteresis-type deep neural network architecture effectively addresses these challenges, reducing long-term stability errors from ±5.0% to ±0.8%, enhancing the reliability of composite sensors under complex working conditions [16-18], and providing accurate data support for wide-range vacuum measurement.

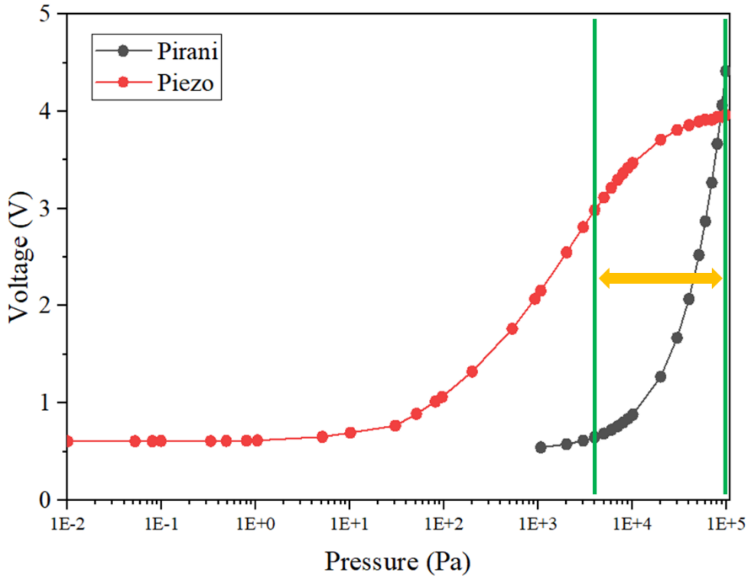

Figure 3. Response data of the composite sensor

3. CALIBRATION ALGORITHM DESIGN AND IMPLEMENTATION

3.1. Calibration Algorithm Framework

In composite sensing systems consisting of Pirani and piezoresistive sensors, traditional calibration algorithms are limited by fixed models and linear assumptions, making it difficult to adapt to sensor nonlinearity and dynamic interference in overlapping regions and complex environments, which leads to reduced measurement accuracy. To overcome this limitation, an adaptive calibration algorithm based on neural networks is adopted. By leveraging the nonlinear fitting and self-learning capabilities of neural networks, this algorithm achieves precise adaptation to complex characteristics (especially in overlapping regions) and environmental interference across the full measurement range [19]. It replaces traditional fixed mathematical models by training neural networks to learn the pressure-voltage characteristics of sensors throughout the full range, adapting to nonlinear and time-varying behaviors. By integrating environmental data such as temperature and gas composition, the neural network autonomously learns the mapping relationship between interference and measurement deviations to compensate for environmental impacts in real time.

The adaptive calibration algorithm framework consists of four core modules: data acquisition, preprocessing, neural network training, and calibration output. T

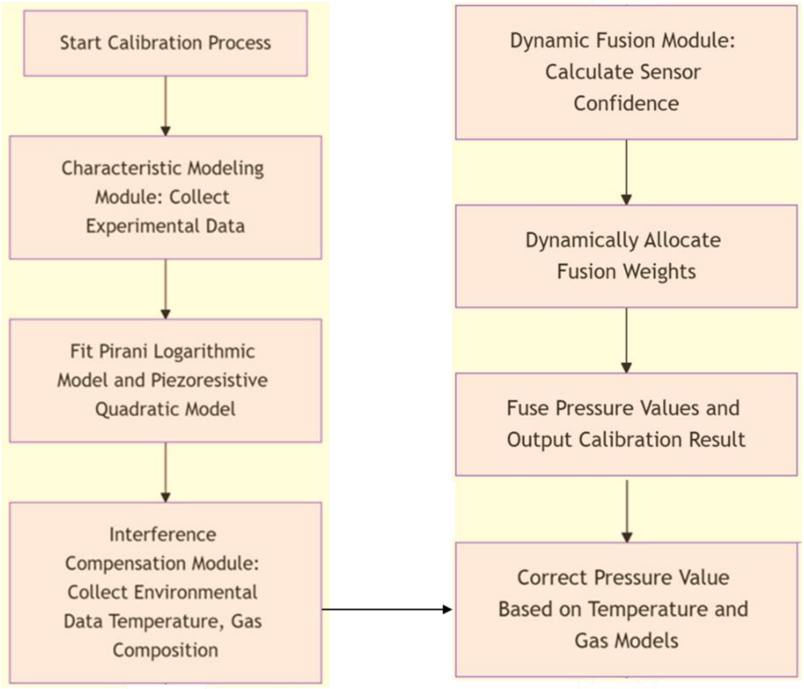

Figure 4. Flowchart of the algorithm framework

3.2. Neural Network

The neural network training module focuses on addressing data jumps in the overlapping segment, environmental interference suppression, and insufficient algorithmic generalization capabilities of wide-range composite vacuum sensors. Its core design objective is to dynamically correct the zero-offset errors of low-precision segments (such as the piezoresistive sensor at the edge of the overlapping region) using the output of high-precision sensors, while optimizing the model parameters of high-precision segments through the stable data of low-precision segments to form a closed-loop calibration mechanism. By integrating environmental parameters such as temperature and gas composition, the neural network learns the nonlinear mapping relationship between sensor outputs and pressure/environmental variables to suppress temperature drift and gas composition interference. Neural network parameters are compressed through model pruning and quantization techniques to adapt to embedded edge hardware, ensuring a calibration delay of <5 ms. The hysteresis-type deep neural network for the overlapping segment proposed in this paper adopts the structure shown in Fig. 5:

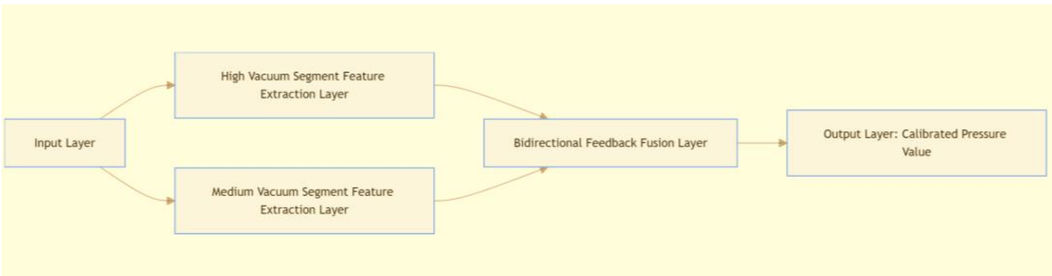

Figure 5. Structure diagram of the neural network

The input layer receives multi-source data, including voltage from the Pirani sensor, voltage from the piezoresistive sensor, temperature T, and gas composition encoding. In the high-vacuum segment (dominated by the Pirani sensor), the feature extraction layer uses a convolutional neural network (CNN) to extract the frequency-domain features of thermal conductivity signals and outputs high-confidence feature vectors. In the medium-vacuum segment (dominated by the piezoresistive sensor), a fully connected layer fits the quadratic nonlinear characteristics of strain signals and outputs feature vectors.

The bidirectional feedback fusion layer consists of forward feedback and backward feedback. The forward feedback uses high-vacuum segment features as a benchmark to generate zero-offset compensation coefficients for the medium-vacuum segment through a long short-term memory network (LSTM) to correct the piezoresistive model. The backward feedback adjusts the model parameters of the high-vacuum segment through an attention mechanism using the corrected stable output of the medium-vacuum segment to suppress temperature drift in the Pirani sensor. The output layer fuses the bidirectional feedback results and outputs calibrated pressure values through a linear layer, with an identity activation function to preserve the linear relationship of physical quantities.

4. MODEL TRAINING AND EXPERIMENTAL VALIDATION

4.1. Model Training

A high-precision vacuum calibration device covering the full measurement range was established. Measurement data from the Pirani and piezoresistive composite sensors were collected at different vacuum levels, with 100 datasets acquired for each vacuum point. The experimental test system is shown in Fig. 6.

A multi-layer perceptron (MLP) was constructed as the training network, with an input layer dimension of 4 corresponding to four normalized features: Pirani voltage, piezoresistive voltage, temperature, and gas thermal conductivity. The network includes 2–3 hidden layers with 64 and 32 neurons respectively, and ReLU activation functions are applied in hidden layers to enhance the network's nonlinear fitting capability. The output layer has a dimension of 1 with a linear activation function, outputting normalized calibrated pressure. Mean squared error (MSE) was selected as the loss function to calculate the normalized error between predicted and standard pressure. The Adam optimizer was used with a learning rate of 0.001 and momentum parameters to adaptively adjust the learning rate for accelerated convergence. The preprocessed dataset was divided into training, validation, and test sets at a ratio of 7:2:1. The training rounds were set to 1,000 with a batch size of 32. Network parameters were iteratively updated on the training set, and overfitting was monitored using the validation set—training would stop early if the validation loss increased for multiple consecutive rounds.

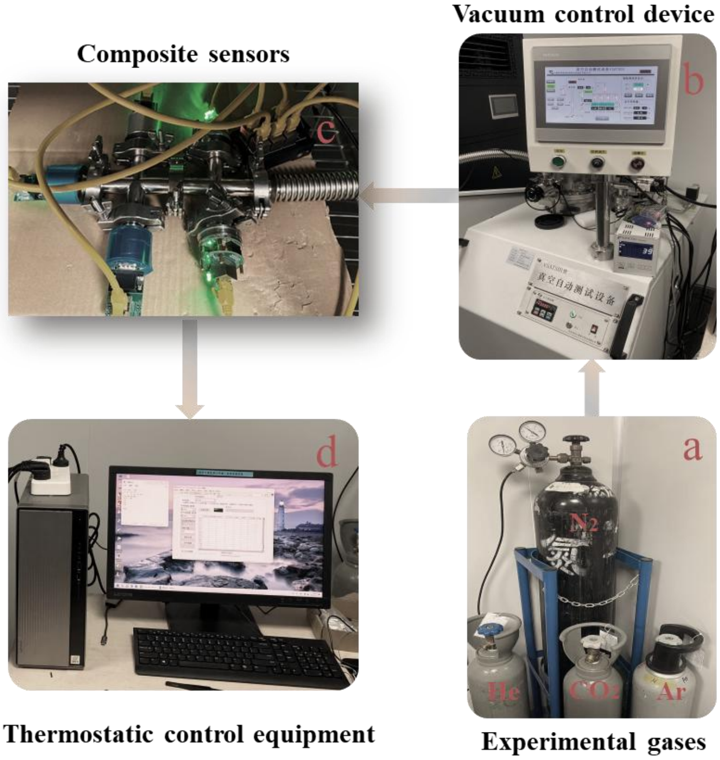

Figure 6. Experimental test system

4.2. Result Analysis

During training, trends in training loss vs. test loss and training accuracy vs. test accuracy were monitored in real time. As shown in Fig. 7, both training and test losses decreased rapidly and stabilized gradually with increasing training rounds, indicating continuous improvement in the network's data fitting performance. Minor fluctuations in the later stage suggest the network's generalization capability on both training and test sets gradually stabilized. Fig. 8 shows that training and test accuracies rose rapidly and approached 1, reflecting continuous improvement in the network's pressure prediction accuracy. Finally, the trained network was used to predict new data, and comparison between predicted and true voltages demonstrated high consistency across the full pressure range (especially in the overlapping region), verifying the model's effectiveness in composite sensor calibration and achieving precise calibration of measurement data from Pirani and piezoresistive sensors. This provides strong support for high-precision vacuum measurement by composite sensors in complex environments.

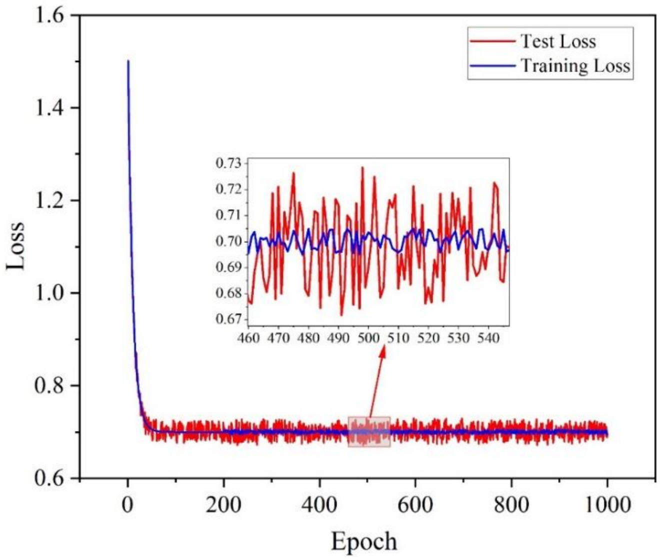

Figure 7. Training and testing Loss

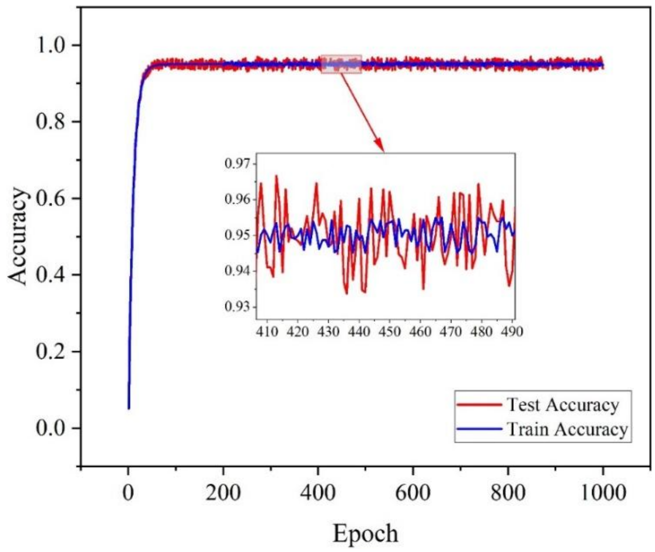

Figure 8. Training and testing accuracy.

As shown in Table 2, calibration tests on validation data revealed that within the overlapping region, the measurement error of the composite sensor was reduced to within ±1% after calibration. In non-overlapping regions, the measurement error in the high-vacuum region (Pirani sensor alone) was ±3%, and that in the low-vacuum region (piezoresistive sensor alone) was ±4%. Compared with pre-calibration results, the full-range measurement accuracy was significantly improved, validating the effectiveness of the calibration algorithm.

Table 2. Data validation results of the composite sensor

Measurement Region	Sensor Operation Mode	Pre-Calibration Error (%)	Post-Calibration Error (%)	Number of Test Samples
Overlapping (50–1000 mbar)	Pirani + piezoresistive	5.2±1.3	0.8±0.2	300
Non-overlapping (<50 mbar)	Pirani	8.5±1.5	3.0±0.5	200
Non-overlapping (>1000 mbar)	Piezoresistive	6.8±1.2	4.0±0.6	250

5. CONCLUSION

This paper investigates calibration algorithms for Pirani-piezoresistive composite sensors, clarifies the characteristics of the overlapping region, and designs and implements a calibration algorithm based on neural networks and polynomial fitting. Through extensive model training and validation, the algorithm effectively improves the measurement accuracy of composite sensors across the full range and addresses the error issue in overlapping data during composite sensor measurement. Future research may further optimize the calibration algorithm to enhance real-time performance and expand the application of composite sensors in more complex environments.

REFERENCES

[1] Grzebyk T, Górecka-Drzazga A. MEMS type ionization vacuum sensor [J]. Sensors and Actuators A: Physical, 2016, 246: 148-155.

[2] Kanda Y, Yasukawa A. Optimum design considerations for silicon piezoresistive pressure sensors [J]. Sensors and Actuators A: Physical, 1997, 62(1-3): 539-542.

[3] Wen X, Chen J, Huang Q, et al. Study of the Effect of Thermal Stress on the Performance of MEMS Pirani Gauges [C]//Journal of Physics: Conference Series. IOP Publishing, 2025, 2982(1): 012011.

[4] Gao Z, Zhou B, Hou B, et al. Self-calibration of nonlinear signal model for angular position sensors by model-based automatic search algorithm [J]. Sensors, 2019, 19(12): 2760.

[5] Jitschin W, Ludwig S. Dynamical behaviour of the Pirani sensor [J]. Vacuum, 2004, 75(2): 169-176.Yan J, Song Z. Metal-decorated 3D tin oxide nanotubes in a monolithic sensor array chip for room-temperature gas identification [J]. Journal of Alloys and Compounds, 2024, 976: 173075.

[6] Romijn J, Dolleman R J, Singh M, et al. Multi-layer graphene pirani pressure sensors [J]. Nanotechnology, 2021, 32(33): 335501.

[7] Toto S, Nicolay P, Morini G L, et al. Design and simulation of a wireless SAW–Pirani sensor with extended range and sensitivity [J]. Sensors, 2019, 19(10): 2421.

[8] Mosser V, Suski J, Goss J, et al. Piezoresistive pressure sensors based on polycrystalline silicon [J]. Sensors and Actuators A: Physical, 1991, 28(2): 113-132.

[9] Tran A V, Zhang X, Zhu B. Mechanical structural design of a piezoresistive pressure sensor for low-pressure measurement: A computational analysis by increases in the sensor sensitivity [J]. Sensors, 2018, 18(7): 2023.

[10] Aryafar M, Hamedi M, Ganjeh M M. A novel temperature compensated piezoresistive pressure sensor [J]. Measurement, 2015, 63: 25-29.

[11] Shi J, Wang L, Dai Z, et al. Multiscale hierarchical design of a flexible piezoresistive pressure sensor with high sensitivity and wide linearity range [J]. Small, 2018, 14(27): 1800819.

[12] Xu S, Yang G, Chen J, et al. Theoretical and experimental investigations of the CMOS compatible Pirani gauges with a temperature compensation model [J]. Microsystems & Nanoengineering, 2025, 11(1): 21.

[13] Yonekura H, Kimura M. Ambient temperature compensation of thin film pirani vacuum sensor [J]. IEEJ Transactions on Sensors and Micromachines, 2007, 127(3): 136-139.

[14] Balderrama V S, Leon-Gil J A, Fernández-Benavides D A, et al. MEMS piezoresistive pressure sensor based on flexible PET thin-film for applications in gaseous-environments [J]. IEEE Sensors Journal, 2021, 22(3): 1939-1947.

[15] Wang X, Que M, Chen M, et al. Full dynamic-range pressure sensor matrix based on optical and electrical dual-mode sensing [J]. Adv. Mater, 2017, 29(15): 1605817.

[16] Moon J, Kim J, Shin Y, et al. Confidence-aware learning for deep neural networks [C]//international conference on machine learning. PMLR, 2020: 7034-7044.

[17] Rossolini G, Biondi A, Buttazzo G. Increasing the confidence of deep neural networks by coverage analysis [J]. IEEE Transactions on Software Engineering, 2022, 49(2): 802-815.

[18] Cortés-Ciriano I, Bender A. Deep confidence: a computationally efficient framework for calculating reliable prediction errors for deep neural networks [J]. Journal of chemical information and modeling, 2018, 59(3): 1269-1281.

[19] Rao A R, Reimherr M. Nonlinear functional modeling using neural networks [J]. Journal of Computational and Graphical Statistics, 2023, 32(4): 1248-1257.